Fluid Drag Reduction by Magnetic Confinement

Arvind Arun Dev,[*,†,‡] Peter Dunne,[†] Thomas M. Hermans,[‡] and Bernard Doudin[*,†]

†*Institut de Physique et Chimie des Matériaux de Strasbourg, UMR 7504 CNRS-UdS, 67034 Strasbourg, France*

‡*Université de Strasbourg, CNRS, UMR 7140, 67000 Strasbourg, France*

E-mail: arvind.dev@ipcms.unistra.fr; bernard.doudin@ipcms.unistra.fr

Abstract

The frictional forces of a viscous liquid flow are a major energy loss issue and severely limit microfluidics practical use. Reducing this drag by more than a few tens of percent remain elusive. Here, we show how cylindrical liquid–in–liquid flow leads to drag reduction of 60–99% for sub-mm and mm-sized channels, regardless of whether the viscosity of the transported liquid is larger or smaller than that of the confining one. In contrast to lubrication or sheath flow, we do not require a continuous flow of the confining lubricant, here made of a ferrofluid held in place by magnetic forces. In a laminar flow model with appropriate boundary conditions, we introduce a modified Reynolds number with a scaling that depends on geometrical factors and viscosity ratio of the two liquids. It explains our whole range of data and reveal the key design parameters for optimizing the drag reduction values. Our approach promises a new route for microfluidics designs with pressure gradient reduced by orders of magnitudes.

Introduction

Friction is a multifaceted problem existing in most physical processes and accounts for almost 25% of energy loss in the world.[1,2] Fluid friction or hydrodynamic viscous drag is decisive when designing energy efficient large scale flow systems.[3] At smaller, microfluidic sizes, channels provide unique advantages for handling small volumes with reduced waste and manufacturing costs, ideal for drug delivery and discovery.[4,5] Flow-focusing using microfluidic channels for drug delivery and chaotic mixing of reactants forms an essential part of pharmaceutical research.[6] However, delivery of highly concentrated drugs through sub-mm diameter medical needles is difficult because of large drag due to the nonlinear increase in viscosity with increasing concentration.[7] This results in pumping forces beyond the range of manual injection.[8] Furthermore, to limit shear damage, aggregation, and sedimentation in medically significant flows, like blood through tubes and arteries,[9] reducing viscous drag is essential. Enabling drag control is also key in studying the response of cancer cells[10] and viruses.[11] Reducing the hydrodynamic viscous drag and shear are key design issues and have led to many solutions, like mixing with additives,[12] surface chemical treatment,[13] or thermal creation of two-phase systems;[14] while Nature's way, the Lotus effect,[15] has steered research towards engineered (super)hydrophobic surfaces[16–18] with stabilized[19,20] liquid/gas interfaces.[21–23] To overcome the drawback of the limited time stability of interstitial gas, oil/liquid infused surfaces have been proposed.[24,25] Establishing liquid walls by means of an interstitial liquid lubricant is of particular interest for microfluidic applications, with several strategies documented in the literature.[26–31] Nanostructured surfaces are shown to enhance lubricant retention thereby extending the lifetime of planar lubricated surfaces.[32] Hydrodynamic fluid focusing and microdroplets microfluidics are designed for surrounding the transported liquid material with an immiscible liquid envelope.[33,34] Core annular flows, where the transported liquid is lubricated coaxially using a liquid of lower viscosity is proposed to handle highly viscous flows in microfluidics.[8] However, forming a stable annular flow is difficult, and the risk of draining the lubricating liquid[35,36] limits the maximum achiev-

able drag reduction. The use of ferrofluids as confining liquid can improve the stability and draining issues, taking advantage of magnets to generate a force field that hold the confining ferrofluid in place. Recent results using ferrofluid-infused surfaces showed superhydrophobic
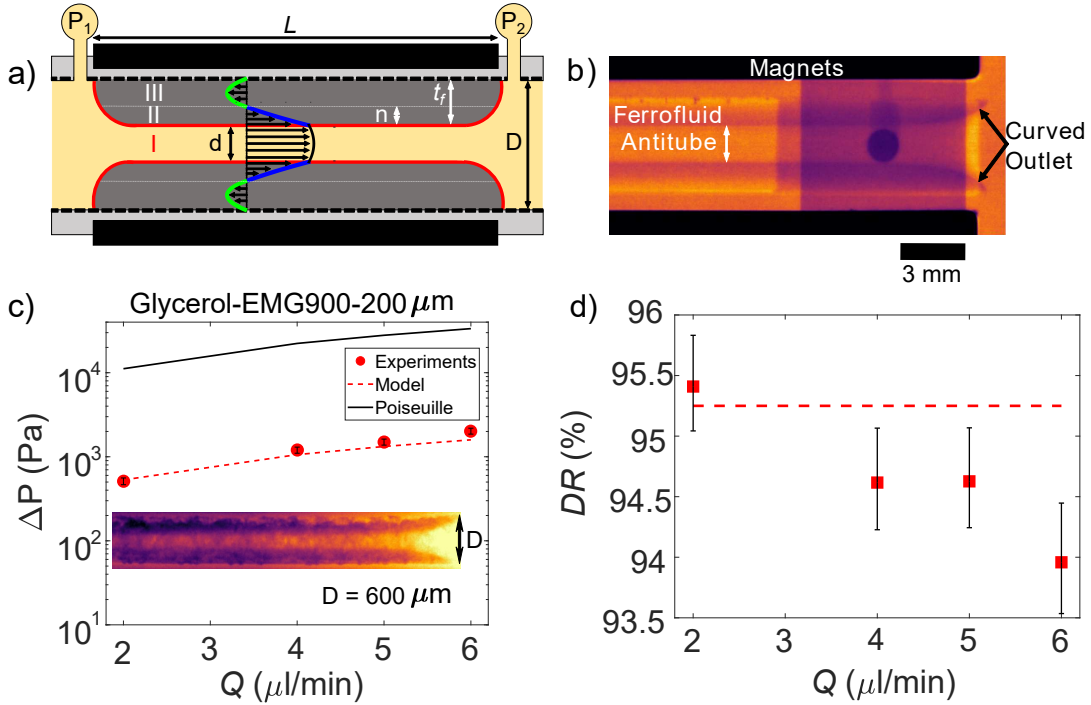
Figure 1: a) Experimental setup for differential pressure measurement (P1, P2). An antitube of diameter d inside a rigid cavity of diameter D is shown with a velocity profile following the hypothesis of a 2-fluid, 3-region model. The red line between the ferrofluid and antitube depicts the liquid-liquid interface. b) X-ray absorption contrast image of the fluidic circuit, inside a cavity surrounded by magnets. The brighter central flowing liquid (antitube) is surrounded by a darker immiscible ferrofluid. c) Pressure-drop versus flow rate for an antitube of diameter 200 μm, with inset showing the X-ray image near the outlet (bright central part is antitube). Markers are experiments, the continuous line is the expectation from a Poiseuille flow of diameter d, and the dashed line is the prediction of the model detailed in the text below. d) Corresponding drag reduction with respect to Poiseuille flow. The viscosity ratio between the transported liquid and the ferrofluid is η_r=11.

behaviour,[37] and early pioneers[38] showed how pressure gradients can be reduced by an intermediate ferrofluid layer in large pipes.[39,40] Here we show how drag reduction, defined as the percentage change in friction factor,[13,23,41–44] is remarkably enhanced in milli- and microfluidic circuits using magnetic confinement of ferrofluid lubricants with appropriate magnet assemblies. Its key element is the implementation of our recent design of quadrupolar confin-

ing magnetic field,[45] capable of stabilizing the cylindrical flow of a diamagnetic liquid (called 'antitube[46]') inside a ferrofluid envelope attracted towards the magnets. Our experimental system forms an ideal liquid–in–liquid tube system where the lubricating liquid forms a perfect concentric confinement for the flowing liquid, using a magnetic force design best suited to preserve the cylindrical geometry and providing optimum robustness of the system. This allows us to compare and verify a simple, axially-symmetric theory with experiments for a significant range of hydrodynamic parameters. The study goes beyond the assumption of unidirectional flow of the involved liquids, ideal for maximum drag reduction.[8,25,29] We previously discussed the expected and measured equilibrium diameter d_{eq} of the antitube under static conditions (no flow), stabilized by the equilibrium between magnetic pressure and surface tension between the liquids.[45] Here we investigate the dynamic case, where the fluid viscosities are key properties, and show how antitube circuits can exhibit drastically reduced pressure drop for significant ranges of viscosity and flow conditions.

Experiments

The fluidic cell design follows our previous work[45] and is sketched in Figure 1a. To perform the flow experiments, the four-magnet assembly were housed in a 3D-printed support with built-in fluidic connectors for pressure measurements (cross-section Fig. 1a). For larger diameter antitubes (> 1 mm) we used a support with a magnet spacing $w = 6$ mm, internal cavity with diameter $D = 4.4$ mm and inlet-outlet separation $L = 52$ mm, and for sub-mm antitube $w = 0.9$ mm, $D = 600$ µm, and $L = 12$ mm. The 3D printed cavity (D, Fig. 1a) is first filled with the non-magnetic liquid, then slowly replaced by injecting the ferrofluid with resulting formation of the antitube.

We control the diameter d, which is always $> d_{eq}$, by varying the injected trapped volume of ferrofluid. We determined the antitube diameter from X-ray absorption contrast images (see supporting information S.I. S1), either with 20 μm resolution setup[45] (Fig. 1b), or a micro

computed tomography system (RX-Solutions EasyTom 150/160) with 6 μm resolution, Fig. 1c inset. The antitube absorbs X-rays less than the ferrofluid, resulting in an image with a bright central region surrounded by two darker bands Fig. 1b). At the top and bottom of the image are the magnets which are opaque to X-rays at this thickness, and appear as two black regions, separated from the ferrofluid by the nearly-invisible 3D printed support. Near the ends of the magnets, the antitubes widen due to the fringe magnetic fields; fortuitously, these curved inlets and outlets improve the trapping of the ferrofluid (see S.I. S1).

We measured the pressure drop, ΔP, between inlet and outlet, with Honeywell pressure transducers (HSCDLND001PG2A3, HSCDLNN400MGSA5) under a constant flow set by a syringe pump (Harvard apparatus PHD 2000). Fig. 1c shows the measured pressure drop as a function of flow rate of glycerol (Sigma Aldrich) flowing through EMG900 (FerroTech) ferrofluid (markers). This pressure drop is more than one order of magnitude lower than a Poiseuille flow in a solid channel with equivalent diameter (200 ± 6 μm). This illustrates how it is beneficial to have a cylindrical flowing liquid confined by a liquid interface rather than by solid walls.

The reduction in pressure drop is better described by the dimensionless friction factor, f. For a fluid with density ρ, the measured pressure drop ΔP resulting from a flow rate Q through a tube of diameter d and length L is related to the experimental friction factor by[23]

$$f_{exp} = \frac{\pi^2 \Delta P d^5}{8 \rho Q^2 L} \tag{1}$$

The drag reduction factor DR is then defined as[13]

$$DR = \frac{f_P - f_{exp}}{f_P} \times 100 \tag{2}$$

which is the percentage change of the measured friction factor f_{exp} compared to the factor f_p under the same flow rate that follows Poiseuille's law. At a solid wall boundary, $f_p = 64/\mathrm{Re}$, where the Reynolds number $\mathrm{Re} = \rho \mathrm{U} d / \eta$ is defined for diameter d, density ρ , viscosity η

and average velocity U corresponding to the flow rate Q. Due to the liquid-liquid interface, the zero-velocity boundary condition at the transported liquid wall (antitube–ferrofluid interface) does not apply, and the deviation from Poiseuille's law results in hydrodynamic drag reduction. Fig. 1d) shows the experimental drag reduction (markers) based on Eq. 1 and Eq. 2 and from data in Fig. 1c), with values reaching 95.5 %. A more complete insight into
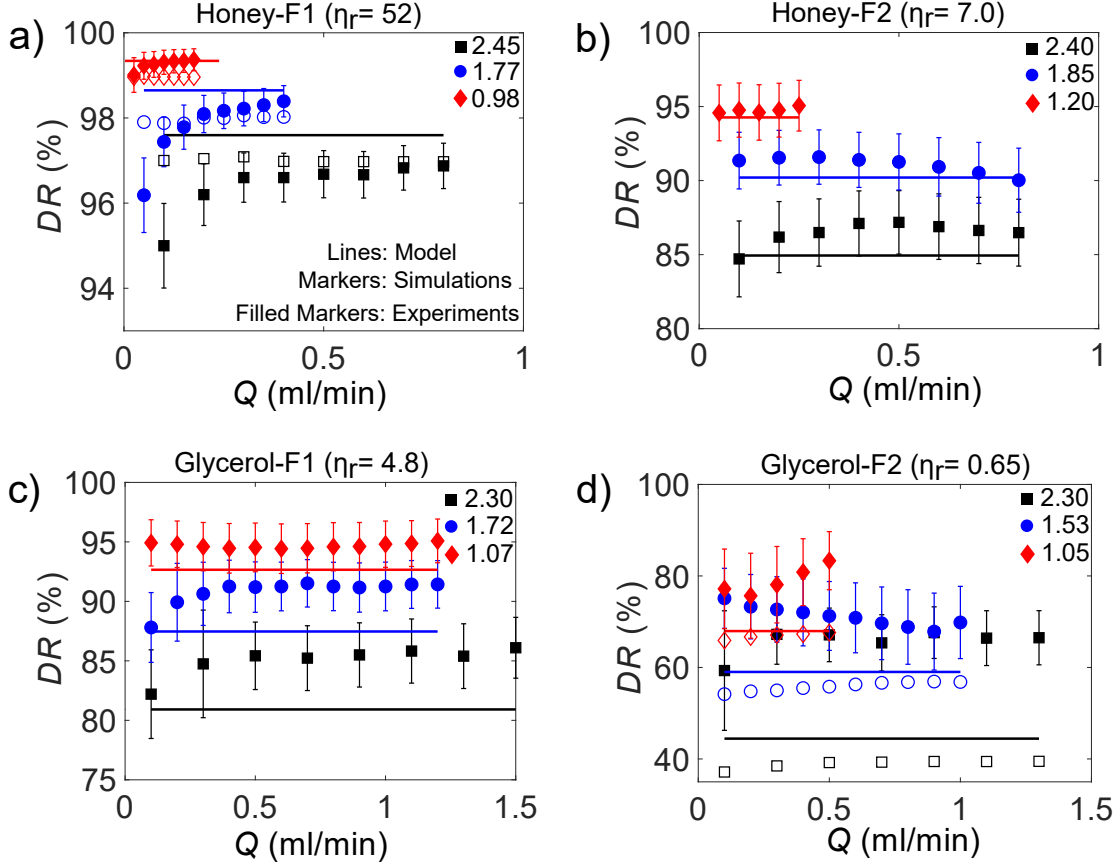
Figure 2: Drag reduction, DR, for three antitube diameters as a function of flow rate for a) honey as the transported liquid with APG314 ferrofluid (F1) as the confining liquid, b) honey with APGE32 ferrofluid (F2), c) glycerol with F1 and d) glycerol with F2. η_r is the ratio between the antitube and ferrofluid viscosities. Legend shows the antitube diameter in mm. Lines, markers and filled markers compare model, simulations, and experiments, respectively.

drag reduction possible values is gained by testing how it evolves under flow when varying the viscosity of both transported and confining liquids as well as the antitube diameter. We limit ourselves to viscous liquids, for measurable pressure differences and investigate

near mm-sized channels for straightforward X-ray imaging. The transported viscous liquids were glycerol (Sigma Aldrich) and honey (Famille Michaud), and the confining ferrofluids used were APG314 (F1) and APGE32 (F2) (FerroTech), resulting in experiments on four combinations of magnetic and non–magnetic liquids.
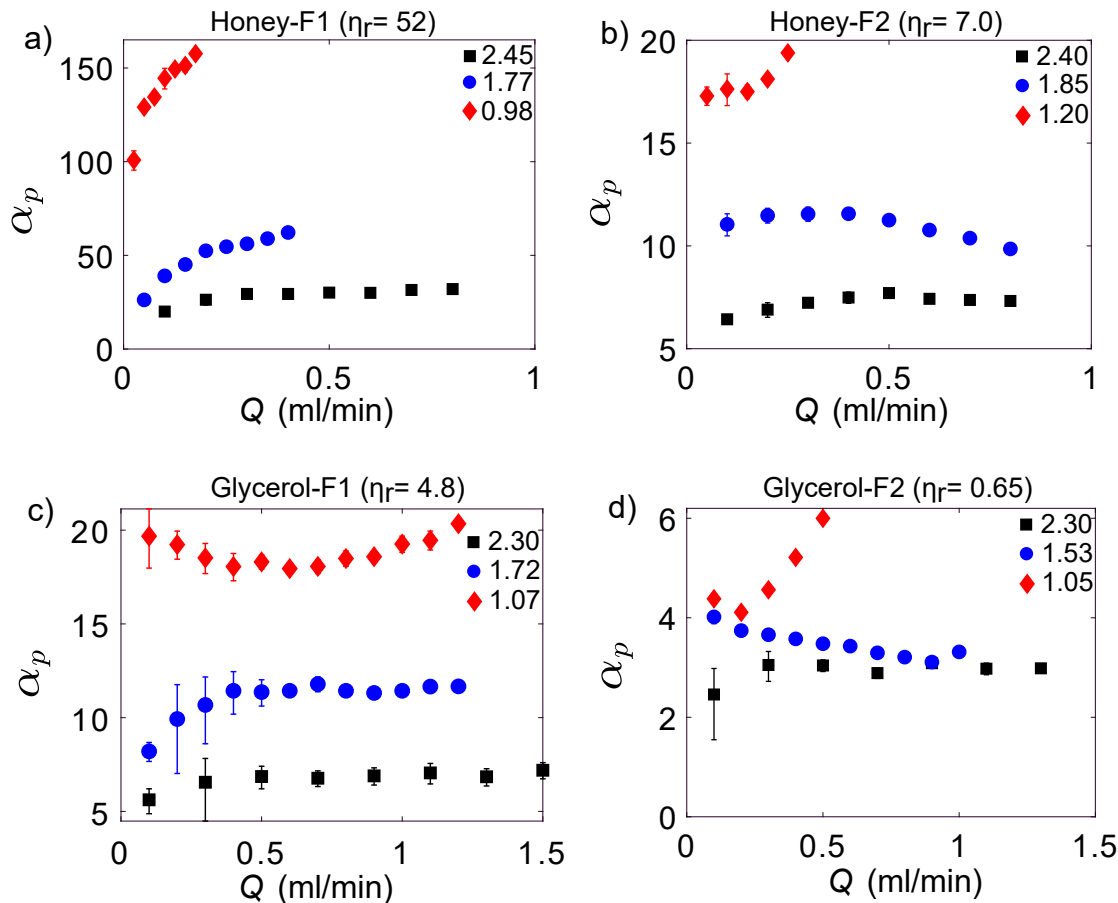
Figure 3: Pressure drop reduction. a) Honey-APG314 (η_r=52), b) Honey-APGE32 (η_r=7.0), c) Glycerol-APG314 (η_r=4.8), d) Glycerol-APGE32 (η_r=0.65). $\alpha_p = \Delta P_{exp} / \Delta P_p$ is the ratio of pressure drop for solid wall tube to the antitube with identical diameter. The error bars are smaller than the size of markers where not visible.

The viscosities of these liquids were measured using a viscometer (Anton Paar MCR 502, see SI S2); for glycerol it is constant at 1.1 Pa.s and for honey 11.99 Pa.s under strain rate of 100 s^{-1} (maximum strain rate in our experiments with honey in antitube is below 10 s^{-1}). Our measurements span a viscosity ratio η_r between transported and confining liquids both larger ($\leq$52) and smaller ($\geq$0.65) than one, with data for three different antitube diameters

and four different viscosity ratios summarized in Fig. 2 and Fig.3.

All 4 combinations of transported and confined liquids show remarkably high drag reductions ranging from 60 % to 99.3 % (Fig. 2). Drag reduction increases with increasing viscosity ratio, with a maximum for Honey-F1 with $\eta_r = 52$ (Fig. 2a). On the contrary, no drag reduction is expected when the ratio goes to zero, describing an infinitely viscous envelope, or a solid wall. However, in contrast to prior expectations,[25] large drag reduction can still be achieved, even if the confining ferrofluid has a larger viscosity than the transported one, such as for Glycerol-F2, where a drag reduction of up to 80% is observed (Fig. 2d). Additionally, the drag reduction increases with decreasing antitube diameter (Fig. 2a,b,c,d), which is beneficial when miniaturizing the fluidic circuit.

Alternatively, the large drag reduction can be expressed as an improvement ratio $\alpha_p = \Delta P_{exp}/\Delta P_p$, which compares the measured pressure drop in a liquid-walled interface, ΔP_{exp}, to a solid-wall interface, ΔP_p, of equivalent diameter, d. Fig. 3 shows more than two orders of magnitude of improvement (α_p) can be achieved. For $\eta_r = 52$, the antitube system results in 157 times less pressure drop than the solid walled tube (Fig. 3a, red markers). Interestingly a viscosity ratio $\eta_r = 0.65$ still results in an almost 6 times smaller pressure drop (Fig. 3d), and the improvement ratio α_p increases with decreasing antitube diameter (Fig. 3a,b,c,d).

Modelling

We explain our results using a two-fluid model, following the previous pioneering works,[40] based on the steady-state one dimensional Navier-Stokes equation with velocity as a function of radius in a cylindrical geometry, $u = u(r)$, under modified boundary conditions. Note that we present below equations that differ from those presented in literature,[40] motivated by the need to compare the analytical expressions to numerical simulations. We checked that the outcomes of both analytical approaches are identical, under the hypothesis of non-deformable interfaces detailed below. A key ingredient of the model is the occurrence of a counter flow

within the confining ferrofluid (Fig. 1a) resulting from avoiding drainage of the ferrofluid by means of the magnetic sources. This suppression is due to the non-uniform magnetic fields at the inlet and outlet opposing any egress of ferrofluid. As the ferrofluid cannot escape but noting that a) flux must be conserved and b) that the drag reduction should result from a non-zero velocity at the ferrofluid-antitube interface, a return path for the ferrofluid flow must exist. The simplest hypothesis is illustrated by the velocity profile in Fig. 1a, where we define three regions: I inside the antitube, II the part of the ferrofluid that travels alongside the antitube flow, and III where counter-flow occurs. The non-dimensional governing equations for the three regions (i = I, II, II) are given by

$$\frac{1}{Re_i \, r^\star} \frac{\partial}{\partial r^\star} \left(r^\star \frac{\partial u_i^\star}{\partial r^\star} \right) = \frac{\partial P_i^\star}{\partial z^\star} \tag{3}$$

where $u_i^\star, r^\star$ are dimensionless velocity and coordinates scaled by the average velocity u_m and the diameter d of the region I (antitube), respectively. The dimensionless pressure is defined as $P_i^\star = P_i / \rho_i u_m^2$ with the corresponding Reynolds numbers for each region being $Re_i = \rho_i u_m d / \eta_i$. Note that the pressure gradients along the main flow in both ferrofluid regions are equal, under the hypothesis that these two regions do not mix, resulting in the absence of pressure gradient along r, and therefore $\frac{\partial P_{II}^\star}{\partial z^\star} = \frac{\partial P_{III}^\star}{\partial z^\star}$.

The magnetic-nonmagnetic interface is modelled as a non-deforming fixed liquid wall. This hypothesis limits us to experiments under low-enough flow values. The case of diameter depending on flow and position along z is beyond the scope and minimal set of hypotheses of this paper, as it is related to the interface stability of non-miscible liquids, and the need to introduce explicitly magnetic stress forces in the model. We checked by X-ray imaging that we are not in this case, aware the deviations for the model will increase with the flow rate, as deformations cannot be neglected anymore.

We assume here that the pressure gradients in regions I and II are different, to ensure a

non-deformable interface. Note that earlier research[40] presented the analytical model as a 2 fluid model with equal pressure gradient, $\frac{\partial P_I^\star}{\partial z^\star} = \frac{\partial P_{II}^\star}{\partial z^\star}$., but since the numerical simulations do not take into account the magnetic forces field, it is essential to define the magnetic-nonmagnetic interface as non-deformable wall resulting in $\frac{\partial P_I^\star}{\partial z^\star} \neq \frac{\partial P_{II}^\star}{\partial z^\star}$. (see section 4 and SI S3). We insist, that so long as the shear stress and velocity boundary conditions at the magnetic-nonmagnetic interface are satisfied, the assumption of pressure gradients do not affect the drag reduction calculations.

Our hypothesis allows us to consider a diameter d, set experimentally by the amount of ferrofluid trapped in the cavity, independent of the flow rate and treat the problem numerically to match our experimental conditions. These governing equations are solved for all velocities ($u_I^\star, u_{II}^\star, u_{III}^\star$), pressure gradient $\frac{\partial P_{III}^\star}{\partial z^\star}$ and thickness n of region II, using boundary conditions depicted in the Fig. 1b: finite velocity at the antitube centre, zero velocity at the solid wall and at interface of II and III, continuity of velocity and shear stress at interfaces I-II and II-III. Along with these boundary conditions, the volume conservation of ferrofluid dictates that the flow rate in region II and III must be equal, $Q_{II}^\star = Q_{III}^\star$. We present two models, one with no assumption (full model) and another with assumption $\frac{\partial P_{II}^\star}{\partial z^\star} = 0$, which explicitly shows the contribution of geometric and fluid parameters for drag reduction. In the full model Eq. 3 expands to

$$\frac{1}{Re_{III}} \frac{1}{r^\star} \frac{\partial}{\partial r^\star} \left(r^\star \frac{\partial u_{III}^\star}{\partial r^\star} \right) = \frac{\partial P_{III}^\star}{\partial z^\star} \tag{4}$$

$$\frac{1}{Re_{II}} \frac{1}{r^\star} \frac{\partial}{\partial r^\star} \left(r^\star \frac{\partial u_{II}^\star}{\partial r^\star} \right) = \frac{\partial P_{II}^\star}{\partial z^\star} \tag{5}$$

$$\frac{1}{Re_I} \frac{1}{r^\star} \frac{\partial}{\partial r^\star} \left(r^\star \frac{\partial u_I^\star}{\partial r^\star} \right) = \frac{\partial P_I^\star}{\partial z^\star} \tag{6}$$

Solving Eq. 4 to Eq. 6 with the boundary conditions mentioned gives the analytical expres-

sions of the flow rate in the antitube as:

$$Q_I^\star = \frac{\pi Re_I}{4} \frac{\partial P_I^\star}{\partial z^\star} \left[\frac{1}{32} + a_3 - a_4 - a_5 \right] \tag{7}$$

and the resulting friction factor written as

$$f_A = 64/Re_I \beta \tag{8}$$

where

$$\beta = 32(a_5 + a_4 - a_3) - 1 \tag{9}$$

and a_3, a_4, a_5 are scalar constants that can be expressed as explicit functions of d, the thicknesses n of the region II and t_f of the ferrofluid.

This 'full model' is therefore fully analytically solvable; however, Eq. 8 and Eq. 9 together presents a complex expression where the contribution of fluid and geometric properties are hidden. Simplified expressions illustrating better the key contributions to drag reduction are obtained by neglecting the pressure gradient in region II. We show below that this artificial hypothesis has limited impact on the accuracy of the results. This approximation $\frac{\partial P_{II}^\star}{\partial z^\star} = 0$ results in a simplified expression for β:

$$\beta_0 = 1 + 4 \ln \left(1 + \frac{2n_0}{d} \right) \eta_r \tag{10}$$

where n_0 is the thickness of the ferrofluid in region II under this approximation. $\eta_r = \eta_a/\eta_f$ is the ratio of viscosity of antitube liquid (η_a) and ferrofluid (η_f). Note that we take the viscosity of the ferrofluid at saturation in a magnetic field (see SI S2). Complete and explicit equations for the scalar constants and simplified model are given SI 4.

4. Numerical visualization of counter flow

Greater confidence in our equations results were gained by computational fluid dynamics (CFD) simulations using ANSYS CFX 18, where detailed information on the occurrence of counter flow and the resulting velocity vector field were obtained. In the numerical simulations, we solve the three-dimensional Navier–Stokes equation by considering the magnetic-nonmagnetic interface as a non-deformable fixed liquid wall of infinitesimal width. The axial velocity and shear stress are equal on both sides of the wall, i.e., continuous across the interface. Since the magnetic field gradient only exists in the radial direction far from the inlet or outlet, no magnetic body force is considered on the ferrofluid. The finite curved edges of ferrofluid near inlet and exit of the flow are modelled as a free slip wall with zero normal velocity (no flow across the curved edges) (See SI S3 for numerical algorithm). The numerical simulations also consider the shear dependent viscosity of ferrofluids. As illustrated in Fig. 4, a counter flow occurs in the ferrofluid close to the outer wall for Honey-F1 with d = 1.73 mm (Fig. 4a) and Glycerol-F2 with d = 1.54 mm (Fig. 4b), and flow rate fixed at Q = 300 μl min^{-1}. Good agreement between numerical and analytical velocity profiles using the full model for both Honey-F1, η_r = 52 (Fig. 4c), and Glycerol-F2,η_r = 0.65, (Fig. 4d) validates our numerical algorithm. To more accurately model the experimental system shown in Fig. 1, we extended the simulations to consider the finite length of a device, and the effect of fringe fields on the shape of interface at the inlet and outlet (curved inlet and outlet, Fig. 1b, see SI S3), beyond the hypothesis of the infinite tube of the analytical model. Numerical simulations were found to reproduce well the drag reduction data in Fig. 2a), while systematically underestimating observed drag reduction for η_r = 0.65 (Fig. 2d). Note that the numerical drag reduction is calculated using Eq. 1 and Eq. 2 with ΔP obtained from numerical simulations.

The simplified model obtained by neglecting pressure gradient term in region II is also compared with the numerical simulations shown in Fig. 4e and Fig. 4f. The difference between the two analytical models is apparent on comparing Fig. 4c with Fig. 4e and Fig. 4d with
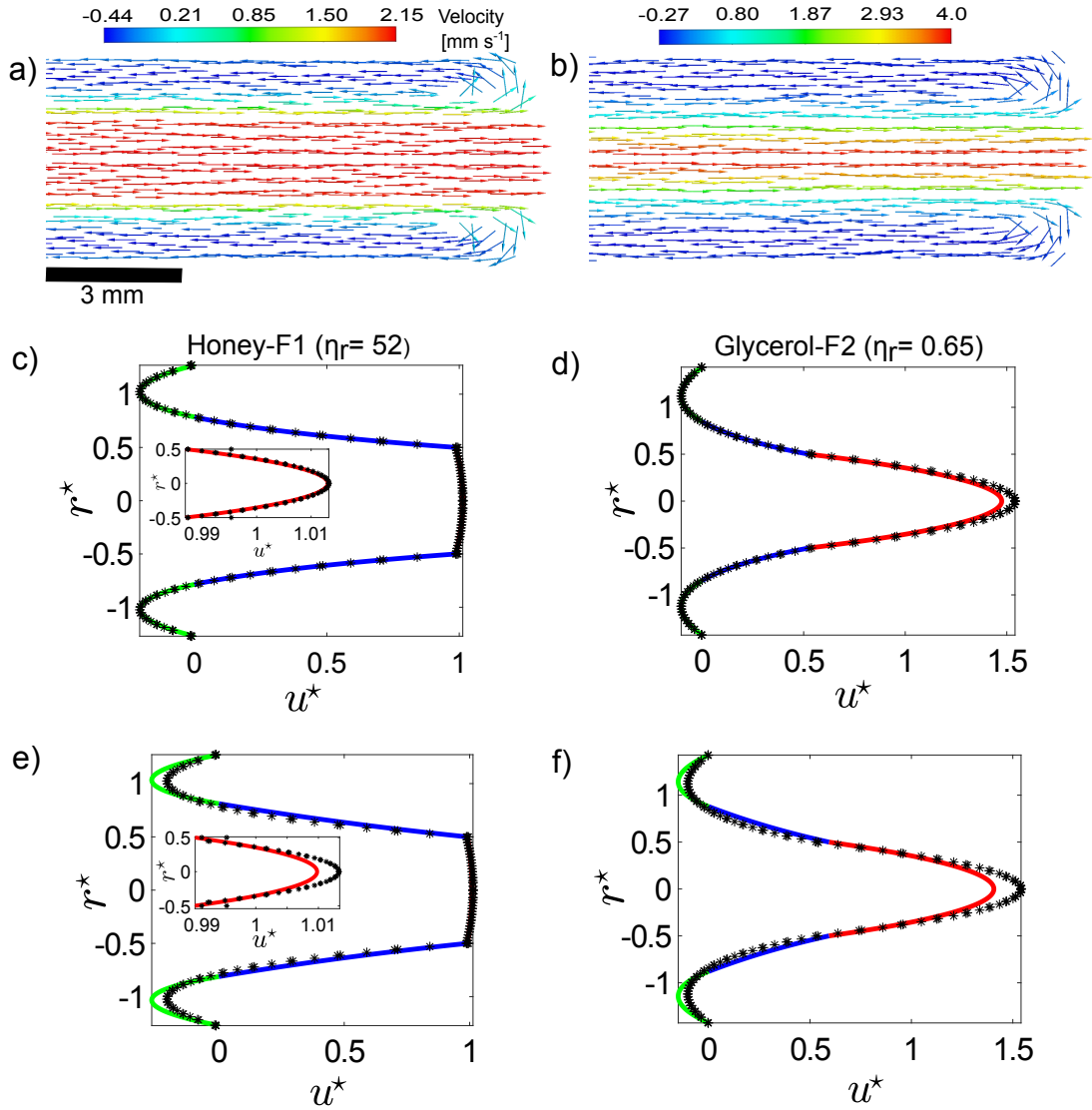
Figure 4: . Simulated visualization of counter flow. a) and b) Velocity vectors near the outlet showing counter flow for Honey-F1 and Glycerol-F2 respectively. c) and d) comparison of the non-dimensional velocity profile of the full analytical model and simulations in Fig. 4(a) and Fig. 4(b). e) and f) comparison using simplified analytical model neglecting pressure gradient term. Lines are model predictions and markers are simulations calculations. Inset shows the magnified view of velocity profile in an antitube. The antitube diameter for left and right column is 1.73 mm and 1.54 mm respectively. η_r is viscosity ratio.

13

Fig. 4f.

Discussion

The analytical model with a minimum set of hypotheses presented here captures reasonably well the experimental measurements for all measurements presented in Fig. 1 and Fig. 2 for mm and sub-mm channels. The modified Reynolds number is the non-dimensional governing parameter and spans four orders of magnitude in our experiments. For a cylindrical tube
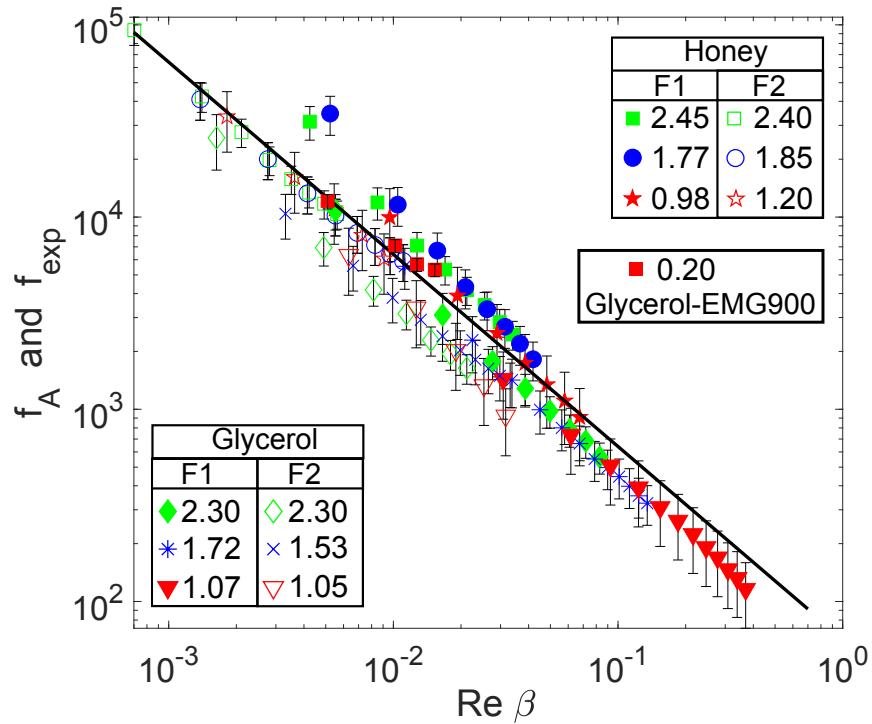
Figure 5: Comparison of experimental fexp (markers) and analytical f_A (line) friction factors. Inset gives the diameter of antitubes (mm) for each case. Re denotes the Reynolds number and β is the scaling factor (= 1 for solid-walled tube).

flow $f = 64/\text{Re}$, the liquid-in-liquid system results in $f_A=64/\text{Re}\beta$ for the same flow rate Q, illustrating how the friction factor is reduced by the scaling factor β. Fig. 5 illustrates how the calculated friction factor f_A which is a function of the modified Reynolds number (from Eq. 3.6) compares with the experimental one f_{exp} computed using Eq. 2.1. The friction factor f_A is like the fit parameter presented in literature.[40] We provide here full

analytical expressions for f_A, necessary for the equation of the drag reduction defined as percentage change in friction factor f_A with respect to friction factor for Poiseuille flow f_p. Similar rescaling of the friction factor was also discussed for a highly water-repellent wall system.[13] Although the model cannot completely account for minor offsets observed at low viscosity ratio values, where deformation of the antitube starts to take place, Fig. 5 nevertheless illustrates the broad range of fluidic conditions that the model can apply to. Note that a significant variation of drag reduction with flow rate is found for the largest viscosity ratio ($\eta_r = 52$). In such cases, the pressure drop becomes very small at small flow rates, and the difficulties in neglecting the pressure loss related to the interconnects and pressure indicators limit the reliability of the data, systematically underestimating the drag reduction values. We also expect that more complicated fluid velocity profiles along z can develop, especially for high viscosity confining liquids where the magnetic/non-magnetic interface might deform significantly due to the high pressure drop but taking them into account is beyond our current model. The simplified expression β_0 in Eq. 10, illustrates the

Table 1: Comparison of the full and simplified models

Case	d (mm)	t_f (mm)	n (mm)	β	n_0 (mm)	β_0
	2.45	0.98	0.34	41.6	0.38	58.68
Honey-APG314	1.77	1.32	0.49	74	0.53	98.3
	0.98	1.71	0.67	151.68	0.73	183.35
	2.40	1.00	0.36	6.74	0.39	9.12
Honey-APGE32	1.85	1.28	0.47	10.21	0.51	13.39
	1.20	1.60	0.61	17.44	0.67	21.49
	2.30	1.05	0.38	5.24	0.41	6.95
Glycerol-APG314	1.72	1.34	0.50	7.98	0.54	10.26
	1.07	1.67	0.65	13.62	0.70	16.46
	2.3	1.05	0.38	1.57	0.41	1.8
Glycerol-APGE32	1.53	1.44	0.54	2.11	0.58	2.44
	1.05	1.68	0.65	2.74	0.71	3.12

deviation from the asymptotic $\beta_0 = 1$ value for solid walls, and is a simple but explicit way to quantify the reduction in the friction resulting from liquid-in-liquid flow. Compared to β, this approximation underestimates the frictional drag (visible in Fig. 4) and becomes more

apparent when the thickness of the ferrofluid decreases (see Table 1). However, β_0, explicitly reveals the contributions of the antitube geometry and fluid properties: the drag reduction can be tuned by the choice of viscosities (η_r) and the amount of ferrofluid trapped in the device cavity, i.e. antitube diameter d, and ferrofluid thickness t_f.

Conclusions

We have studied the flow of viscous liquids through cylindrical liquid-in-liquid tubes where the confining liquid is held in place by a quadrupolar magnetic field. Our results show that drag reductions exceeding 99% can be achieved by exploiting the non-zero velocity of a viscous liquid at its interface with the encapsulating liquid. The friction reduction is quantified by rescaling of the Reynolds number with a factor β in Eq. 9. The drag reduction improves when decreasing the diameter of an antitube relative to its surrounding ferrofluid, or when increasing the ratio of the antitube to ferrofluid viscosities. The former is relevant for the needs and length-scales of microfluidics, while the latter indicates that large drag reduction is expected when flowing highly viscous liquids. Moreover, with antitube diameters as small as 10 μm already achievable,[45] antitube diameter to ferrofluid thickness ratios of order 100 are within reach. Therefore, very large drag reduction in microfluidic channels is possible for a broad range of confining liquid viscosities. Downsizing or designing magnetic force gradients along the flow direction can also further enhance the stability of the ferrofluid against shearing, paving the way to both high velocity and low viscosity fluidic applications in domains ranging from nanofluidics to marine or hydrocarbon cargo transport.

Acknowledgement

Supporting Information Available

The supporting information consist of a PDF document with

- Procedures for characterising antitube diameters.

- Viscosity measurements of antitube liquids and confining ferrofluids.

- Numerical simulation procedures and flow chart.

- Details of analytical model used in this article.

References

(1) Sayfidinov, K.; Cezan, S. D.; Baytekin, B.; Baytekin, H. T. Minimizing friction, wear, and energy losses by eliminating contact charging. *Science Advances* **2018**, *4*.

(2) Holmberg, K.; Erdemir, A. Influence of tribology on global energy consumption, costs and emissions. *Friction* **2017**, *05*, 263.

(3) Brostow, W. Drag reduction in flow: Review of applications, mechanism and prediction. *Journal of Industrial and Engineering Chemistry* **2008**, *14*, 409 – 416.

(4) Dittrich, P.; Manz, A. Lab-on-a-chip: microfluidics in drug discovery. *Nature reviews. Drug discovery* **2006**, *5*, 210–8.

(5) Neuži, P.; Giselbrecht, S.; Länge, K.; Huang, T.; Manz, A. Revisiting lab-on-a-chip technology for drug discovery. *Nature reviews. Drug discovery* **2012**, *11*, 620–32.

(6) Damiati, S.; Kompella, U. B.; Damiati, S. A.; Kodzius, R. Microfluidic Devices for Drug Delivery Systems and Drug Screening. *Genes* **2018**, *9*.

(7) Sharma, V. K.; Patapoff, T. W.; Kabakoff, B.; Pai, S.; Hilario, E.; Zhang, B.; Li, C.; Borisov, O.; Kelley, R. F.; Chorny, I.; Zhou, J. Z.; Dill, K. A.; Swartz, T. E. In silico selection of therapeutic antibodies for development: Viscosity, clearance, and chemical stability. *Proceedings of the National Academy of Sciences* **2014**, *111*, 18601–18606.

(8) Jayaprakash, V.; Costalonga, M.; Dhulipala, S.; Varanasi, K. K. Enhancing the Injectability of High Concentration Drug Formulations Using Core Annular Flows. *Advanced Healthcare Materials* **2020**, *9*, 2001022.

(9) Reinke, W.; Gaehtgens, P.; Johnson, P. C. Blood viscosity in small tubes: effect of shear rate, aggregation, and sedimentation. *American Journal of Physiology-Heart and Circulatory Physiology* **1987**, *253*, H540–H547.

(10) Mitchell, M. J.; King, M. R. Computational and Experimental Models of Cancer Cell Response to Fluid Shear Stress. *Frontiers in Oncology* **2013**, *3*, 44.

(11) Grein, T. A.; Loewe, D.; Dieken, H.; Weidner, T.; Salzig, D.; Czermak, P. Aeration and Shear Stress Are Critical Process Parameters for the Production of Oncolytic Measles Virus. *Frontiers in Bioengineering and Biotechnology* **2019**, *7*, 78.

(12) Lee, S.; Spencer, N. D. Sweet, Hairy, Soft, and Slippery. *Science* **2008**, *319*, 575–576.

(13) Watanabe, K.; Udagawa, Y.; Udagawa, H. Drag reduction of Newtonian fluid in a

circular pipe with a highly water-repellent wall. *Journal of Fluid Mechanics* **1999**, *381*, 225–238.

(14) Saranadhi, D.; Chen, D.; Kleingartner, J. A.; Srinivasan, S.; Cohen, R. E.; McKinley, G. H. Sustained drag reduction in a turbulent flow using a low-temperature Leidenfrost surface. *Science Advances* **2016**, *2*.

(15) Ensikat, H.; Ditsche-Kuru, P.; Neinhuis, C.; Barthlott, W. Superhydrophobicity in perfection: the outstanding properties of the lotus leaf. *Beilstein Journal of Nanotechnology* **2011**, *2*, 152–161.

(16) Tuo, Y.; Zhang, H.; Rong, W.; Jiang, S.; Chen, W.; Liu, X. Drag Reduction of Anisotropic Superhydrophobic Surfaces Prepared by Laser Etching. *Langmuir* **2019**, *35*, 11016–11022.

(17) Ko, Y. S.; Kim, H. J.; Ha, C. W.; Lee, C. Quantifying Frictional Drag Reduction Properties of Superhydrophobic Metal Oxide Nanostructures. *Langmuir* **2020**, *36*, 11809–11816.

(18) Shirtcliffe, N. J.; McHale, G.; Newton, M. I.; Zhang, Y. Superhydrophobic Copper Tubes with Possible Flow Enhancement and Drag Reduction. *ACS Applied Materials & Interfaces* **2009**, *1*, 1316–1323.

(19) Carlborg, C. F.; van der Wijngaart, W. Sustained Superhydrophobic Friction Reduction at High Liquid Pressures and Large Flows. *Langmuir* **2011**, *27*, 487–493.

(20) Pinchasik, B.-E.; Wang, H.; Möhwald, H.; Asanuma, H. Fully Reversible Transition between Cassie and Wenzel States via Acoustic Waves. *Advanced Materials Interfaces* **2016**, *3*, 1600722.

(21) Hu, H.; Wen, J.; Bao, L.; Jia, L.; Song, D.; Song, B.; Pan, G.; Scaraggi, M.; Dini, D.;

Xue, Q.; Zhou, F. Significant and stable drag reduction with air rings confined by alternated superhydrophobic and hydrophilic strips. *Science Advances* **2017**, *3*.

(22) Choi, C.-H.; Kim, C.-J. Large Slip of Aqueous Liquid Flow over a Nanoengineered Superhydrophobic Surface. *Phys. Rev. Lett.* **2006**, *96*, 066001.

(23) Karatay, E.; Haase, A. S.; Visser, C. W.; Sun, C.; Lohse, D.; Tsai, P. A.; Lammertink, R. G. H. Control of slippage with tunable bubble mattresses. *Proceedings of the National Academy of Sciences* **2013**, *110*, 8422–8426.

(24) Wong, T.-S.; Kang, S. H.; Tang, K. Y. S.; Smythe, E. J.; Hatton, B. D.; Grinthal, A.; Aizenberg, J. Bioinspired self-repairing slippery surfaces with pressure-stable omniphobicity. *Nature* **2011**, *477*, 443–447.

(25) Solomon, B.; Khalil, K.; Varanasi, K. Drag Reduction using Lubricant-Impregnated Surfaces in Viscous Laminar Flow. *Langmuir : the ACS journal of surfaces and colloids* **2014**, *30*.

(26) Sharma, H.; Gaddam, A.; Agrawal, A.; Joshi, S. Slip flow through microchannels with lubricant-infused bi-dimensional textured surfaces. *Microfluidics and Nanofluidics* **2019**, *23*, 1–13.

(27) Hou, X.; Li, J.; Tesler, A.; Yao, Y.; Wang, M.; Min, L.; Sheng, Z.; Aizenberg, J. Dynamic air/liquid pockets for guiding microscale flow. *Nature Communications* **2018**, *9*.

(28) Darvishi, S.; Cubaud, T. Lubrication of Highly Viscous Core-Annular Flows in Microfluidic Chambers. *Journal of Fluids Engineering* **2011**, *133*, 031203.

(29) Walsh, E.; Feuerborn, A.; Wheeler, J.; Tan, A.; Durham, W.; Foster, K.; Cook, P. Microfluidics with fluid walls. *Nature Communications* **2017**, *8*.

(30) Scarratt, L. R. J.; Zhu, L.; Neto, C. How Slippery are SLIPS? Measuring Effective Slip on Lubricated Surfaces with Colloidal Probe Atmoc Force Microscopy. *Langmuir* **2019**, *35*, 2976–2982.

(31) Scarratt, L.; Zhu, L.; Neto, C. Large Effective Slip on Lubricated Surfaces Measured with Colloidal Probe AFM. *Langmuir* **2020**, *36*.

(32) Laney, S. K.; Michalska, M.; Li, T.; Ramirez, F. V.; Portnoi, M.; Oh, J.; Thayne, I. G.; Parkin, I. P.; Tiwari, M. K.; Papakonstantinou, I. Delayed Lubricant Depletion of Slippery Liquid Infused Porous Surfaces Using Precision Nanostructures. *Langmuir* **2021**, *37*, 10071–10078.

(33) Rajawat, A.; Tripathi, S. Disease diagnostics using hydrodynamic flow focusing in microfluidic devices: Beyond flow cytometry. *Biomedical Engineering Letters* **2020**,

(34) Baroud, C.; Gallaire, F.; Dangla, R. Dynamics of microfluidic droplets. *Lab on a chip* **2010**, *10*, 2032–45.

(35) Wexler, J. S.; Jacobi, I.; Stone, H. A. Shear-Driven Failure of Liquid-Infused Surfaces. *Phys. Rev. Lett.* **2015**, *114*, 168301.

(36) Peppou-Chapman, S.; Neto, C. Depletion of the Lubricant from Lubricant-Infused Surfaces due to an Air/Water Interface. *Langmuir* **2021**, *37*, 3025–3037.

(37) Wang, W. et al. Multifunctional ferrofluid-infused surfaces with reconfigurable multiscale topography. *Nature* **2018**, *559*, 77–82.

(38) Medvedev, V.; Krakov, M. Flow separation control by means of magnetic fluid. *Journal of Magnetism and Magnetic Materials* **1983**, *39*, 119 – 122.

(39) Medvedev, V.; Krakov, M.; Mascalik, E.; Nikiforov, I. Reducing resistance by means of magnetic fluid. *Journal of Magnetism and Magnetic Materials* **1987**, *65*, 339 – 342.

(40) Krakov, M. S.; Maskalik, E. S.; Medvedev, V. F. Hydrodynamic resistance of pipelines with a magnetic fluid coating. *Fluid Dynamics* **1989**, *24*, 715–720.

(41) Fukuda, K.; Tokunaga, J.; Nobunaga, T.; Nakatani, T.; Iwasaki, T.; Kunitake, Y. Frictional Drag Reduction with Air Lubricant Over a Super-Water Repellent surface. *Journal of Marine Science and Technology* **2000**, *5*, 123–130.

(42) Mirbod, P.; Wu, Z.; Ahmadi, G. Laminar flow drag reduction on soft porous media. *Scientific Reports* **2017**, *7*.

(43) Liu, W.; Ni, H.; Wang, P.; Zhou, Y. An investigation on the drag reduction performance of bioinspired pipeline surfaces with transverse microgrooves. *Beilstein Journal of Nanotechnology* **2020**, *11*, 24–40.

(44) Ayegba, P. O.; Edomwonyi-Otu, L. C.; Yusuf, N.; Abubakar, A. A review of drag reduction by additives in curved pipes for single-phase liquid and two-phase flows. *Engineering Reports* **2020**, e12294.

(45) Dunne, P.; Adachi, T.; Dev, A. A.; Sorrenti, A.; Giacchetti, L.; Bonnin, A.; Bourdon, C.; Mangin, P. H.; Coey, J. M. D.; Doudin, B.; Hermans, T. M. Liquid flow and control without solid walls. *Nature* **2020**, *581*, 58–62.

(46) Coey, J. M. D.; Aogaki, R.; Byrne, F.; Stamenov, P. Magnetic stabilization and vorticity in submillimeter paramagnetic liquid tubes. *Proceedings of the National Academy of Sciences* **2009**, *106*, 8811–8817.